

Electric Drive Systems with Long Feeder Cables

Patrick Xie^{1*}, Gaurang Vakil¹, and Chris Gerada¹

¹Power Electronics, Machines and Control Research, University of Nottingham, Nottingham, United Kingdom

*E-mail: patrick.xie@nottingham.ac.uk

Accepted to IET Electric Power Applications on 30th July 2019

Abstract

Electric drive systems with long feeder cables connecting inverter and machine are used for oil exploration, mining, remote operated vehicles, industrial, and aerospace applications. Though this topology has the advantage of providing a better operating environment and easier serviceability for the inverter if the machine is located in an inhospitable and inaccessible environment, it does come with its own drawbacks. Steep-fronted switched voltages and cable-machine surge impedance mismatch can lead to high-amplitude, high-frequency (HF) voltage oscillations along the feeder cable, at the machine terminals, and throughout the machine's stator windings. These effects can cause high EMI, corona discharge, insulation failure in the feeder cable and machine's stator windings, common-mode, differential-mode, and bearing currents. This paper discusses the HF issues relating to electric drive systems with long cable feeders. HF models for feeder cable and machine to analyse these phenomena are presented. The effects on long feeder cable loading on inverter switching characteristics are discussed. Methods to mitigate high-amplitude and HF oscillations in such systems are shown.

1 Introduction

Consider an electric drive system where the inverter and machine are separated by a long feeder cable. This arrangement is suitable for applications where the machine is operating in an inhospitable/difficult-to-access location while the inverter is in a better, more easily accessible and serviceable operating environment [1]. However, such set-ups comes with its drawbacks. Steep-fronted high dv/dt switched voltages from the inverter and cable-machine surge-impedance mismatch can cause high-amplitude, HF voltage oscillations along the cable, at the machine terminals and throughout the stator windings [2]. High-amplitude HF voltage oscillations can cause problems such as partial discharge leading

to the breakdown of cable [3] and machine winding insulation [4], and ultimately failure of the drive system. Environmental operating conditions need to be taken into consideration with regards to calculating the partial discharge inception voltage (PDIV) and insulation sizing. High-amplitude HF voltage oscillations can also cause HF common-mode (CM) current, differential-mode (DM) current, bearing current leading to bearing failure, and EMI.

Mitigation of high-amplitude and high-frequency voltage oscillations can reduce and/or eliminate all the problems related to it. Because these phenomena are HF phenomena, HF cable feeder models and HF machine models are required.

In this paper, example applications involving long feeder cables are mentioned in Section 2. The issues and problems related to the electric drives with long feeder cables are discussed in Section 3. Various HF models for feeder cables are presented in Section 4. High frequency machine models are shown in Section 5. The effects of cable loading on inverter switching characteristics is presented in Section 6. Solutions to mitigate high-amplitude and high-frequency voltage oscillations due to long feeder cable loading are discussed in Section 7.

2 Applications

Applications for electric drive systems with long feeder cables include oil exploration [5], mining [6], remote operated vehicle [7], industry [8], and aerospace. [9] analyses a deep-ocean crude-oil pumping application where the system under study consists of an electrical submersible pump with a 75kW induction machine located at the ocean bed, connected to the inverter at sea-level via a step-up transformer and a 1.6km feeder cable. The development of an out-runner PMSM connected to a long cable for a flying remote operated vehicle (ROV) is described in [7] where the considered ROV has a maximum altitude of 300 metres with a 2.6kW PMSM fed from a VSI with a 560V dc link bus. The aviation industry has been advancing towards a more electric aircraft (MEA) [10] to improve performance while decreasing operating and maintenance costs, and reduce carbon emissions. The adoption of electrical actuation to replace hydraulic actuation systems for flight controls and landing gear is currently being investigated [11]. An example application is a distributed electromechanical actuator system for slat/flap actuation [12] where instead of multiple slats that are mechanically coupled and driven by a single hydraulic actuator, multiple distributed electrical actuators are used on the slats, leading to reduced mass and installation effort.

3 Background and Issues

In this section, the background of high-amplitude, high frequency voltage oscillations and transmission line effects due to long feeder cable loading are described and introduced. This is followed by the issues related to and caused by the high

amplitude, high frequency voltage oscillations.

3.1 High-amplitude, High Frequency Voltage Oscillations

In the most basic form, the high-amplitude HF voltage oscillations present in a electric drive systems with long feeder cables and switched voltage source can be demonstrated using a two-port lossless transmission line connected to a voltage source and switch, representing the inverter, and a load, to represent the machine. The surge-impedance of the load Z_L is assumed to be very high compared to that of the source impedance Z_S . The lossless transmission line can be defined by its characteristic impedance Z_0 , and cable length l_c . When the switch closes, a voltage step is applied to the feeder cable and an incident voltage front propagates along it at a velocity of propagation $v = 1/\sqrt{LC}$, where L and C are the per unit length inductance and capacitance of the transmission line respectively. The load side reflection coefficient Γ_L is the ratio of the reflected to incident wave and calculated as,

$$\Gamma_L = \frac{Z_L - Z_0}{Z_L + Z_0}. \quad (1)$$

Because $Z_L \gg Z_0$, Γ_L is approximately equal to 1 and all of the incident voltage wave front is reflected back to the inverter, leading to a doubling of voltage on the load side. The voltage wave front continue to reflect back and forth along the cable between the inverter and machine load, causing voltage oscillations. The frequency of these voltage oscillation f at a given point on the transmission line is,

$$f = \frac{v}{4l_c} = \frac{1}{4l_c\sqrt{LC}}. \quad (2)$$

For the case of a lossy system with a finite surge load impedance, the oscillations eventually decay. However, if another voltage pulse is applied before these oscillations decay sufficiently, the machine terminal can reach up to three times that of the inverter's DC link voltage [13].

Fig. 1 illustrates a case of high amplitude, HF voltage oscillations due to transmission line effects in an electric drive system with a 100m long feeder cable and 1-hp induction machine taken from [2]. The voltage at the inverter side, middle of the feeder cable, and at the machine terminal side are measured. While the inverter voltage is 300V, the peak transient machine terminal voltage is nearly twice that at 570V. The frequency of the voltage oscillations estimated from the plot is 300kHz.

3.2 Issues related to high amplitude, high frequency voltage oscillations

Repeated high-amplitude voltage oscillations can cause partial discharge leading to breakdown of cable [3] and stator winding insulation [4]. The partial discharge inception voltage (PDIV) is the voltage at which electric discharge partially

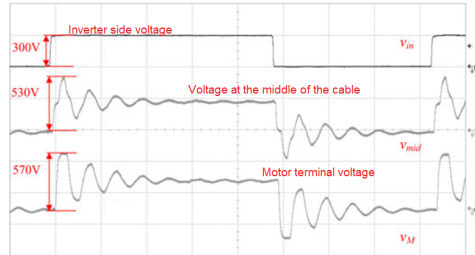


Figure 1: Example of high amplitude, high frequency voltage oscillations due to the transmission line effects in a drive system with 100m long feeder cable. (y-axis: 300V/div, time base: 6 μ s/div). [2]

bridges the insulation. These discharges can be seen as sparks arcing in air between two points and can cause excess heating and damage of solid insulation. This phenomenon can be seen in Fig. 2 (a) where turn-to-turn partial discharge activity is shown [14]. If the amplitude of the voltage oscillations exceed the PDIV at every inverter switching event and the inverter is switching at several kHz's, partial discharge also occurs at every switching event, leading to rapid deterioration of the solid insulation. [8] describes the case of a turn-to-turn short in a 7kW induction machine caused by antiresonance phenomenon due to poor pairing of feeder cable with machine as shown in Fig. 2 (b). Despite the fact, the machine's voltage rating is 460V and its peak insulation voltage rating is 1600V, its stator winding insulation still failed due to this phenomenon.

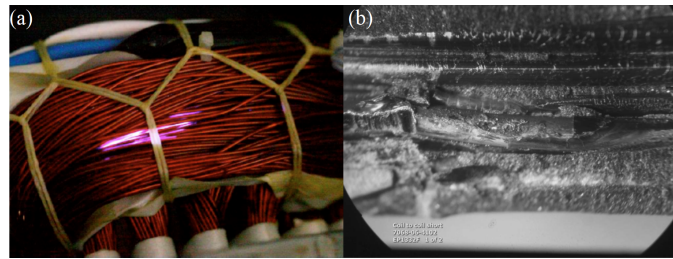


Figure 2: Stator insulation damage, (a) partial discharge activity in the stator [14]. (b) turn-to-turn failure in the 7kW PM machine due to the antiresonance phenomenon [8].

The conditions for partial discharge to occur depends on pressure and temperature. The breakdown voltage in air as a function of the product of pressure and gap distance is conventionally determined using Paschen's law and corrected for temperature using the Peek [16] or Dunbar correction factor [17]. As pressure reduces, so too does the breakdown voltage. For example, breakdown voltages across a 1mm gap as determined using Paschen's law at ground level

100kPa, and 40,000ft at 18.75kPa are 4.5kV and 1.6kV respectively. [18] observed deviations between the experimentally measured breakdown voltages and calculated values from the conventional Paschen's law and with the Peek and Dunbarr correction factors applied, for non-atmospheric pressures and temperature deviations.

High-amplitude HF voltage oscillations due to switched inverters with long feeder cables can cause HF CM current, bearing currents and bearing failure. A study by EASA (Electrical Apparatus Service Association) stated that 51% of faults in electric machines are related to bearings [1] [19] with 9% of bearing failures caused by bearing currents [20]. Common-mode voltage and current are naturally generated from PWM inverters. Because switched three-phase voltages are used, the resultant sum of the three phase voltages, known as the CM voltage, is non-zero and has values of thirds of the DC link voltage for a two-level inverter. This CM voltage is applied to the distributed capacitive couplings between the inverter, cable, and machine with respect to ground and generates the HF CM current in these paths. Common-mode current excites a circumferential HF CM flux around the machine shaft induces a voltage along the shaft, leading to bearing currents [21]. The two kinds of bearing currents are conduction current and discharge current. These discharges damage the bearings and its race surface [22]. Fig. 3 shows fluting or "stretch marks" seen on the race surface is characteristic to that of bearing current damage.



Figure 3: Damaged outer race of bearing due to bearing currents. [15]

Oscillatory voltages, CM currents, and DM currents can cause excess unwanted EMI. More demanding environments, such as defence [23] and aerospace [24] [25], with potentially sensitive electronic equipment have stringent EMC requirements.

Mitigation of high-amplitude and high-frequency voltage oscillations will reduce and/or eliminate all their related problems such as partial discharge, EMI, bearing currents, insulation breakdown, CM and DM voltages and currents. Because these phenomena are HF phenomena, HF cable feeder models, and HF machine models are required.

4 Long Feeder Cable Models

In this section, different HF models for long cable feeders are presented. These models extend upon the standard feeder cable model by including the associated behaviour of the open circuit impedance, skin effect, proximity effect and

impedance frequency-dependence. They can be used to model transmission line effects and high-amplitude high-frequency voltage oscillations. Experimental, analytical, and FEA methods to determine the feeder cable HF model parameters are shown.

4.1 Single-line Transmission Line Models

The single-line transmission line cable model are commonly used for modelling high frequency transmission line effects in machine drive systems. The justification of using single-line instead of multi-line transmission line models is conventional two-level inverter's switching schemes would result in connecting two of its output phases to one polarity of the inverter's dc bus and the remaining phase is connected to the opposite polarity.

Transmission lines can be modelled by distributed parameter or lumped parameter models. In a distributed parameter model, the transmission line is divided into an infinite number of infinitesimally short segments to represent the distributed series resistance R and inductance L , and parallel capacitance C and conductance G , expressed in ohms, henries, farads and siemens per unit length (PUL) respectively as shown in Fig. 4 (a). The telegrapher's equation describes the voltage V and current I on a transmission line with respect to time t and position z .

$$\frac{\partial V(z, t)}{\partial z} = -(R + j\omega L)I(z, t), \quad (3)$$

$$\frac{\partial I(z, t)}{\partial z} = -(G + j\omega C)V(z, t), \quad (4)$$

Analysis based on the telegrapher's equation is limited by the assumption that resistance and inductance are constant at all frequencies which, in reality, vary at high frequency due to skin effect and proximity effect. Lumped parameter models can take these frequency dependent effects into consideration by the addition of extra components to each line segment and are more simply solved using circuit theory.

For a lumped parameter model, the transmission line of length l_c is divided into a finite N number of short line segments of length $\Delta z = l_c/N$, each segment's impedance approximated by series resistance and inductance, and parallel capacitor and resistor as seen in Fig. 4 (b).

To determine the number of line segments N required to model up to the highest harmonic f_{co} , consider the minimum wavelength λ_{min} of the highest harmonic f_{co} is,

$$\lambda_{min} = \frac{1}{f_{co}\sqrt{LC}}. \quad (5)$$

The minimum segment length should be at least a tenth of the minimum wavelength [29]. Thus,

$$N = \frac{l_c}{\lambda_{min}/10} = 10l_c f_{co}\sqrt{LC}. \quad (6)$$

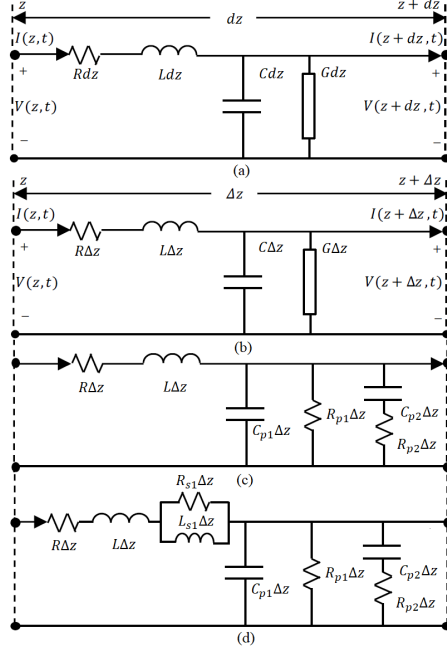


Figure 4: Single line high frequency feeder cable segment models, (a) distributed parameter model [26], (b) lumped parameter model, (c) lumped parameter model considering open circuit impedance [27], (d) lumped parameter model considering open circuit impedance, skin effect and proximity effect[28].

[27] extends upon the standard lumped parameter model as seen in Fig. 4 (b) by adding additional circuit components to the transversal path as seen in Fig. 4 (c). The transversal parameters $R_{p1}, R_{p2}, C_{p1}, C_{p2}$ represent the behaviour of the open circuit impedance. [28] extends upon Fig. 4 (c) to include skin and proximity effects represented by high-order branches R_{s2}, L_{s2} as seen in Fig. 4 (d). To determine the parameters of the respective equivalent circuit, short circuit and open circuit impedance measurements are taken of the cable as shown in Fig. 5. The respective impedance plots can be seen in Fig. 6 and Fig. 7. The parameters of the lumped parameter model are fitted to the measured impedance plots using their respective circuit parameter equations as derived in their respective papers [27] and [28].

4.2 Multi-line Transmission Line Model and Modal Decomposition

Fig. 8 provides a representation of the three-phase line segment by lumped parameter elements. The longitudinal and transversal resistance, inductance, and capacitance parameters of the line segment can be presented in matrix

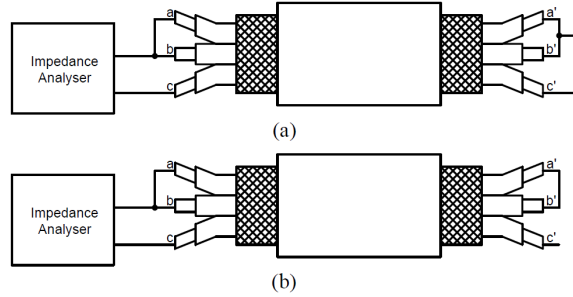


Figure 5: Cable impedance measurement. (a) Short circuit. (b) Open circuit.

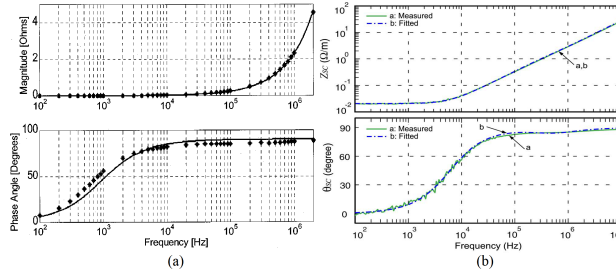


Figure 6: Short circuit impedance results for equivalent circuits in (a) Fig. 4 (b) (dots: measured, line: fitted)[27] and (b) Fig. 4 (c) (line: measured, dotted: fitted)[28].

form as shown in (7), (8), and (9) respectively [30]. Transversal conductance is ignored in this model.

$$[R] = \begin{bmatrix} R_{11} & R_{12} & R_{12} \\ R_{12} & R_{11} & R_{12} \\ R_{12} & R_{12} & R_{11} \end{bmatrix} \quad (7)$$

$$[L] = \begin{bmatrix} L_{11} & L_{12} & L_{12} \\ L_{12} & L_{11} & L_{12} \\ L_{12} & L_{12} & L_{11} \end{bmatrix} \quad (8)$$

$$[C] = \begin{bmatrix} C_{11} & C_{12} & C_{12} \\ C_{12} & C_{11} & C_{12} \\ C_{12} & C_{12} & C_{11} \end{bmatrix} \quad (9)$$

In the frequency domain, longitudinal impedance $[Z]$ and transverse admittance $[Y]$ can be presented as,

$$[Z] = [R] + j\omega[L] \quad (10)$$

$$[Y] = j\omega[C] \quad (11)$$

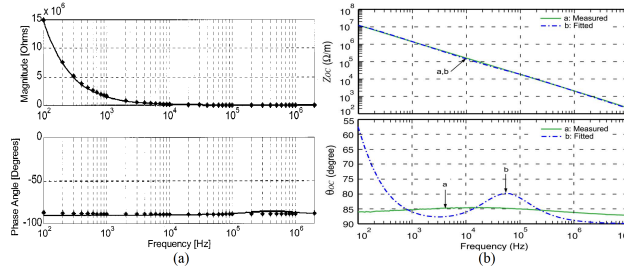


Figure 7: Open circuit impedance results for equivalent circuits in (a) Fig. 4 (b) (dots: measured, line: fitted)[27] and (b) Fig. 4 (c) (line: measured, dotted: fitted)[28].

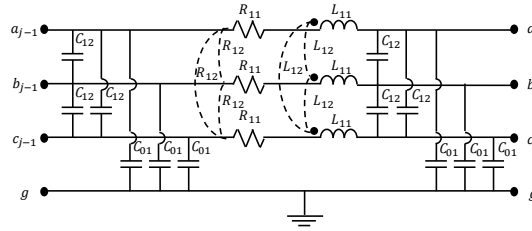


Figure 8: Representation of a line segment by discrete circuit elements. [30]

where ω is the electrical angular speed. Applying modal decomposition to (10) and (11) gives the line parameters in the modal domain as follows,

$$[Z_m] = [R_m] + j\omega[L_m] = [T_V]^{-1}[Z][T_I], \quad (12)$$

$$[Y_m] = j\omega[C_m] = [T_I]^{-1}[Y][T_V], \quad (13)$$

where the transformation matrix $[T_I]$ is equal to the Clarke's transform and $[T_V]$ is the transpose of $[T_I]$. The coupled three-phase transmission line representation is transformed to a modal representation with three uncoupled modes α , β , and 0. Each mode can be represented by a π equivalent circuit as seen in Fig. 9, thus simplifying the simulation the process. Voltages and currents in three-phase domain can be transformed in and out of the modal domain using the transforms $[T_I]$ and $[T_V]$.

$$[Z_m] = \begin{bmatrix} Z_\alpha & 0 & 0 \\ 0 & Z_\beta & 0 \\ 0 & 0 & Z_0 \end{bmatrix} \quad (14)$$

$$[Y_m] = \begin{bmatrix} Y_\alpha & 0 & 0 \\ 0 & Y_\beta & 0 \\ 0 & 0 & Y_0 \end{bmatrix} \quad (15)$$

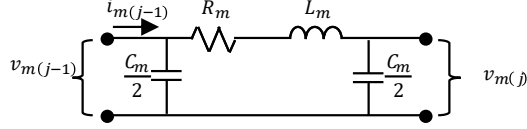


Figure 9: Line segment representation in modal domain. [30]

4.3 Vector Fitting

Vector fitting [31] [32] is used in [33] and [34] to fit a rational approximation transfer function in the frequency domain to measured short circuit and open circuit impedance data using poles and residues. It is a pole relocation technique where the poles are iteratively improved in a least squares manner until convergence is achieved. This technique can be used for high order systems across a wide range of frequencies, making it ideal for wideband modelling of network equivalents, transformers and transmission lines. The rational approximation transfer function $f(s)$ to be fitted is as follows,

$$f(s) = \sum_{m=1}^N \frac{r_m}{s - a_m} + d + se \quad (16)$$

VF identifies the poles a_m and residues r_m of $f(s)$ in a least-squares sense.

This method of fitting has been shown to be accurate, robust and efficient.

[26] and [33] uses VF to fit longitudinal parameters for the single-line case. The longitudinal impedance $Z(\omega)$ can be represented as follows,

$$Z(\omega) = R_{dc} + j\omega F(\omega). \quad (17)$$

An expression for $Z(\omega)_{\text{fit}}$ used to fit $Z(\omega)$ can be written as,

$$Z(\omega)_{\text{fit}} = R_{dc} + j\omega p + \sum_{i=1}^m \frac{j\omega c_i}{j\omega - a_i}. \quad (18)$$

It can be seen that (18) has a similar form to (16). Vector fitting can be used to fit $Z(\omega)_{\text{fit}}$ to $Z(\omega)$. Assuming that the fitted poles a_i and residues c_i are real, an equivalent RL-network can be generated as shown in Fig. 10 and expressed as follows,

$$Z(\omega)_{\text{fit}} = R_0 + j\omega L_0 + \sum_{i=1}^m \frac{j\omega R_i}{j\omega + (R_i/L_i)}. \quad (19)$$

Because the use of an RL-network only allows the use of real poles and residues in the fitting, the complex terms are discarded which in turn effects accuracy. [34] and [35] extends this RL model by using an RLC-network to

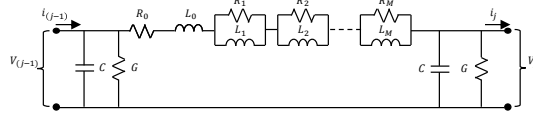


Figure 10: π circuit with RL-network presenting frequency single-phase line. [33]

include complex poles and zeros in the fitting as seen in Fig. 11 using the expression as shown,

$$\begin{aligned}
 Z(\omega)_{\text{fit}} = & R_d c + j\omega p + \sum_{q=1}^N \frac{p_q}{j\omega - a_q} \\
 & + \sum_{b=N+1}^{N+M} \left(\frac{s_{br} + js_{bi}}{j\omega + g_{br} - jg_{bi}} + \frac{s_{br} - js_{bi}}{j\omega + g_{br} + jg_{bi}} \right).
 \end{aligned} \tag{20}$$

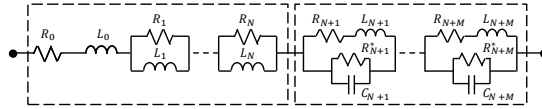


Figure 11: π circuit with RLC-network presenting frequency single-phase line. [34]

It can be used to simulate fast and slow transients and steady state operation. Fig. 12 shows simulated voltage at the receiver end during connection and disconnection of a capacitor bank.

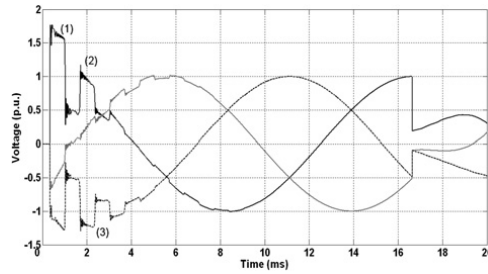


Figure 12: Simulated voltage with mixed fast and slow transients with steady state signal. [33]

4.4 Determination of transmission line parameters

The use of an impedance analyser to experimentally determine the the impedance characteristics has been presented in Fig. 5. During the design phase, there are two ways in which the PUL high frequency transmission line parameters can be determined, using analytical equations or finite element analysis. A review of both approaches is presented here.

4.4.1 Analytical Equations

Consider determining the discrete circuit elements of the multi-line segment representation in Fig. 13. The per-line PUL DC series resistance can be calculated as,

$$R_{11_DC} = \frac{\rho}{A}, \quad (21)$$

where ρ is the conductivity of the conductor and A is its cross-sectional area. Skin effect needs to be considered at high frequency. As frequency increases, skin depth δ reduces as shown,

$$\delta = \sqrt{\frac{2}{\omega\sigma\mu}}, \quad (22)$$

where ω is the electrical angular speed, σ is the conductivity and μ is magnetic permeability. Assuming a circular cross-sectional conductor of radius r , the PUL ac resistance can be determined as follows,

$$R_{11_AC} = \frac{(2r)^2 R'_{dc}}{(4r - \delta)\delta}. \quad (23)$$

The PUL conductance G is determined as follows,

$$G = \frac{1}{R_{12}} = C\omega \tan(\text{DF}), \quad (24)$$

where $\tan(\text{DF})$ is the dissipation factor which is the ratio of traversal equivalent series resistance and the capacitive reactance.

The expressions for PUL self and mutual inductance L_{11} and L_{12} for low frequency (LF) and high frequency (HF) are as follows [36],

$$L_{11_LF} = \frac{\mu_0}{\pi} \left(\ln \frac{2a}{d} + \frac{\mu_r}{4} \right), \quad L_{11_HF} = \frac{\mu_0}{\pi} \left(\ln \frac{2a}{d} \right), \quad (25)$$

$$L_{12_LF} = \frac{\mu_0}{2\pi} \left(\ln \frac{2a^2}{dr_1} + \frac{\mu_r}{4} \right), \quad L_{12_HF} = \frac{\mu_0}{2\pi} \left(\ln \frac{2a^2}{dr_1} \right), \quad (26)$$

where the dimensions a , d , and r_1 are shown in Fig. 14 (a).

The analytical PUL phase-to-ground capacitance expressions for C_{10} and phase-to-phase capacitance C_{12} for a three-conductor cable as shown in Fig. 14 (b) determined using the mirror image method are as follows [37],

$$C_{10} = 2\pi\epsilon \frac{1}{\ln \frac{16a(b^3 - a^3)}{3D^3d}}, \quad (27)$$

$$C_{12} = 2\pi\epsilon \frac{\ln \frac{4a(a^2+b^2+ab)}{3D^2}}{\ln \frac{12a^2(b-a)^2}{d^2(a^2+b^2+ab)} \ln 2 \frac{16a(b^3-a^3)}{3D^3d}}, \quad (28)$$

where $b = D^2/(4a)$ and dimensions D , d , a , r_1 are shown in Fig. 14 (a).

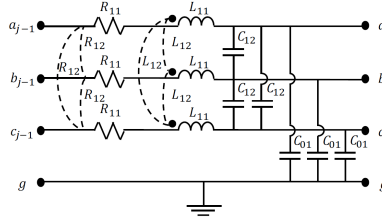


Figure 13: Three-phase Γ transmission line circuit. [37]

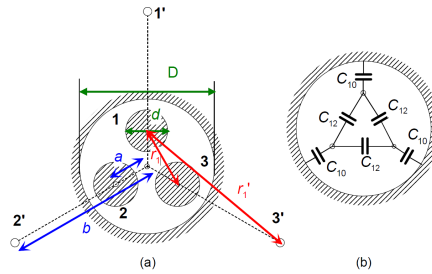


Figure 14: Three-phase cable dimensions. (a) Mirror images. (b) Partial capacitances. [37]

To determine the self and mutual inductances, phase-to-phase and phase-to-ground for cables with more than three conductors, consult [36] [37].

The shortcomings of using analytical equations in determining PUL parameters are shown in [38] where analytically determined PUL cable parameters as calculated and compared with measured values at 500kHz for a three-phase unshielded cable. Here, a large discrepancy between the measured and analytically determined resistance is observed as proximity effect is not considered in the analytical calculation.

4.4.2 FEA

Finite-Element Analysis (FEA) can be used to determine the PUL parameters of a cable and address a lot of the short comings of using analytical equations by considering proximity effect, skin effect, eddy current and complex geometry. The potential of FEA determination of PUL cable parameters for time-domain modelling of transmission line effects and HF high amplitude voltage oscillations is shown in [39]. Its results showed FEA determined values within 5-10% of measured RLC cable parameters and time-domain simulation results of CM

current, DM current, voltage overshoot and ringing within 7-15% of experimentally measured values.

The non-linear partial differential equations governing the electromagnetic field for a cable are as follows [40],

$$\vec{\nabla} \times \left(\frac{1}{\mu} \cdot \vec{\nabla} \times \vec{A} \right) = \vec{J}, \quad (29)$$

$$\nabla \cdot \left(\frac{\partial \vec{A}}{\partial t} \nabla V \right) = 0, \quad (30)$$

where μ is the magnetic permeability, \vec{A} is the magnetic vector potential, \vec{J} is the total current density, σ is the electric conductivity and V is the electric scalar potential.

The capacitance values are determined by solving the electrostatic problem as defined by the following Maxwell equation,

$$\nabla \cdot (\epsilon \nabla V) = -\rho, \quad (31)$$

where ϵ is permittivity, V is the electric scalar potential and ρ is the surface charge density. The mutual and ground capacitance is determined for each line. A unit charge is applied to one conductor while the other conductor's potential is calculated to determine mutual and ground capacitance. Fig. 15 shows the distortion of the equipotential lines due to the proximity of conductors.

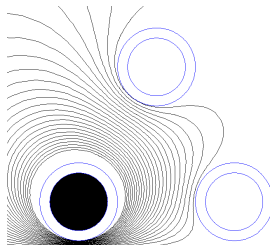


Figure 15: Equipotential line distortion in cable due to conductor proximity. [41]

Skin effect, proximity effect and cable geometry can be taken into consideration when using FEA. Proximity effect is the influence of alternating current in one conductor on the current distribution of another nearby conductor. In [41], comparisons were made between the proximity effect and cables across a range of dimensions. It is observed that the proximity effect increases at higher frequencies, is more prominent in cables with larger cross sections/gauges and increases as the distance between conductors decreases. Inductance varies only slightly at high frequencies due to proximity effect. Capacitance is strongly influenced by the geometry and relative spacing of conductors and observed not to vary with frequency [38][39]. The influence of proximity effect and skin effect

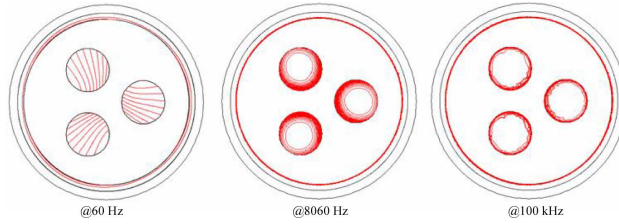


Figure 16: Cable current density distribution at different frequencies. [44]

on the cable current density distribution can be seen in Fig. 16. The contours represent current density of equal magnitude.

Different considerations can be taken for the boundary condition considering the cable's design and operating environment. For armoured/screened cables, a Dirichlet boundary condition can be adopted on the outer surface of the cable whereby a zero magnetic potential is established [41]. For unscreened cables, the earth plane/operating environment needs to be considered. If the cable is located in a metallic cable tray, an ideal earth plane can be considered as the current return path [41]. If the cable's operating location has non-ideal low conductivity, such as in earth, soil stratification model can be used, each layer with different electromagnetic properties [42]. Thermal ratings of underground power cables may also need to be taken into consideration [43].

After determining the PUL cable parameters as a function of frequency, an equivalent cable model can be developed.

5 High Frequency Machine Models

In this section, a variety of high frequency machine models are presented. These include lumped equivalent circuits, that can model CM, DM and bearing currents, and stator windings transmission line models that model stator winding voltage distribution and inter-turn stator voltage reflections during transience. Experimental and FEA based methods can be used to determine the parameters of these models and equivalent circuits.

5.1 Distributed equivalent circuit

Surge voltage distribution within the stator winding can be analysed by modelling it using discrete RLC network elements [45] [46]. Each turn can be represented by its inductance l_t , resistance r_t , turn-to-ground capacitance C_g and turn-to-turn capacitance C_t as seen in Fig. 17. When a voltage step is applied to the input terminal of the winding, the voltage is not instantaneously evenly distributed across all turns along the winding due to the presence of C_g and C_t . If the voltage across the turn-to-turn capacitance is initially zero and the turn-to-ground capacitance is at ground potential, the full input voltage can be seen across the first turn while the remaining turns of the winding remain at

ground potential. As current starts to flow from the first turn to the second turn through l_t and r_t , C_g of the next turn can start to charge up. As current starts to flow in through all of the turns, voltage will eventually be evenly distributed throughout the winding. The presence of LC networks can cause turn-to-turn voltage oscillations.

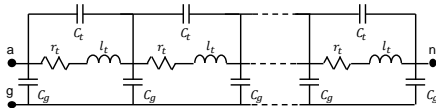


Figure 17: Distributed LC network model of multi-turn winding. [45]

Different stator coil winding schemes need to be considered such as form wound and mush wound. Form wound machines tend to be higher voltage, their coils are wound in an ordered manner, their conductor dimensions are uniform and each turn is laid in succession to each other. Mush wound machines are lower voltage machines where the turns can be randomly arranged.

[45] determines the stator winding per turn discrete RLC network values, in the absence of FEA, as a function of frequency for a mush wound machine on an average basis as shown below,

$$r_t = R_c/N, \quad (32)$$

$$l_t = \frac{L_c}{N^2}, \quad (33)$$

$$M = k\sqrt{L_1L_2}, \quad (34)$$

$$C_{tg} = C_{cg}/N, \quad (35)$$

where N is the number of turns in the coil, R_c is the total resistance of the coil, L_c is the total inductance of the coil, M is the mutual inductance, k is the coupling coefficient assumed to be 0.8 - 0.9, L_1 and L_2 are the leakage inductances of each turn/coil, C_{cg} and C_{tg} are the total coil to ground and the average turn-to-ground capacitance respectively.

[47], [48], [49], and [50] analysed surge voltage distribution and inter-turn voltage reflection of a stator winding by modelling it as multi-conductor transmission line model. Consider the stator winding with n number of coils in four different regions as seen in Fig. 18. These regions are the front overhang, the upper-slot, the lower slot and the rear overhang zones. The conductors in the portion of winding in each region are coupled together and can be represented by a multi-conductor transmission line with its own impedance characteristics and specific boundary conditions. Because the characteristic impedance of the multi-conductor transmission line model in the overhang and in the slots are mismatched, inter-turn and inter-regional voltage reflections can occur and can be modelled and analysed using this technique.

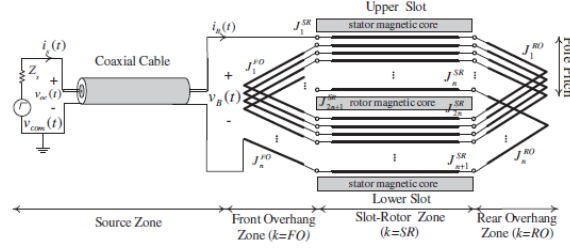


Figure 18: Stator winding model considering overhang and slot regions. [47]

5.2 Lumped equivalent circuits

HF lumped equivalent circuits models for machines are presented. These equivalent circuits include parameters that represent the parasitic capacitance between stator winding and machine frame, neutral and machine frame, grounding resistance of the machine frame, high frequency resistance of the winding, leakage inductance of the winding and parasitic inductance.

The parameters for the lumped equivalent circuits can be determined from FEA models or from machine common-mode and differential-mode impedance measurements using an impedance analyser as seen in Figure 19.

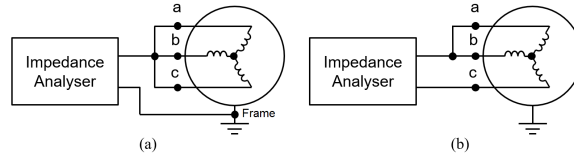


Figure 19: Machine impedance measurement. (a) Common-mode impedance. (b) Differential-mode impedance.

Measured machine impedance values from [51] are shown in Figure 20 for 240kW induction machine. For the common-mode impedance amplitude plot, two anti-resonance and one resonance points are observed within the range of 1kHz to 10MHz.

[52] proposes a per-phase HF equivalent circuit induction machine model in Fig. 21 (a) where R represents the stator and rotor phase resistance, L_d is the phase leakage inductance, C_t is the turn-to-turn distributed capacitive coupling, C_g is the winding-to-ground distributed capacitive coupling and R_e is the eddy currents in the magnetic core and frame. The phase terms R and L_d are low frequency (LF) values, as determined using the locked rotor test at 50/60Hz. The two capacitors C_g , representing distributed winding-to-ground, are both the same value, one is connected between the phase input and ground and the other is connected to neutral to ground. The eddy current resistance R_e describes the losses of eddy currents and adds additional damping at high frequency. This model showed good results up to 1MHz where it was able to

accurately capture one of the first resonance point in the machine’s impedance characteristic.

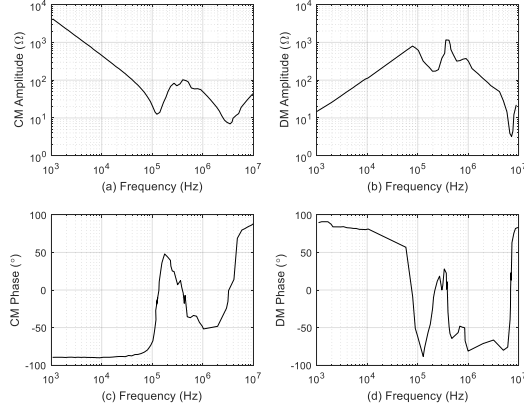


Figure 20: Measured impedance plots of 240kW induction machine. (a) Common-mode impedance amplitude. (b) Common-mode impedance phase. (c) Differential-mode impedance amplitude. (d) Differential-mode impedance phase. [51]

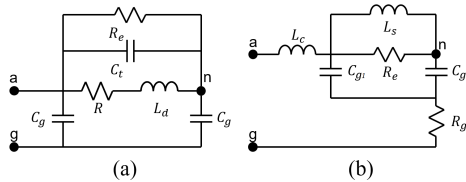


Figure 21: Per-phase high-frequency equivalent circuit from (a) [52], (b) [51].

[51] proposes a HF per-phase machine model for modelling CM current, as seen in Fig. 21 (b). It has reduced parameters and complexity compared to [27] while still able to capture the first two resonance points in the machine impedance characteristic within the 10kHz-10MHz range. L_c is the inductance of connectors and internal line conductors. The winding-to-stator frame capacitance is represented by two separate capacitances, C_{g1} and C_{g2} , and share a common path to ground through resistor R_g . R_g is the dissipative losses caused by the CM current flowing through the stator. It is assumed that the HF components of the supply voltage only effect the first few turns of a winding due to the presence of distributed turn-to-turn capacitance along the stator winding. Thus, the winding-to-stator stray capacitance of the first few turns C_{g1} , is a low impedance path in the HF range. The remainder of the winding represents the LF characteristics as LF components of the supply voltage can further

penetrate into the winding. This consists of the eddy current loss resistance R_e and stator leakage inductance L_s . The lumped stator frame-to-stator winding capacitance $C_{g1} + C_{g2}$ describes the LF characteristics. The proposed HF per-phase machine model [51] in Fig. 21 (b) is verified against a range of induction machines from 1.5kW to 240kW by comparing measured and calculated impedance characteristics and measured and simulated CM currents. The calculated CM machine impedance characteristics agreed well with the measured characteristic as there is an accurate match of the resonance and antiresonance points. There is notable discrepancies in the DM impedance characteristics, particularly in the LF region. Simulation of the CM current were completed in the time domain and verified against drive systems with switched voltages and varying cable lengths. The accuracy of the time domain simulation results is related to the calculated fit of the measured CM impedance. If the measured CM machine impedance characteristic has two distinct antiresonance points and one distinct resonant point, the proposed model can fit this easily. However, if additional minor resonance/antiresonance points are present, this model would not be able to capture these characteristics and the resultant time domain CM current simulation would be less accurate.

[27] extends upon the model proposed in [52] as seen in Fig. 22 (a). At higher frequencies, more resonances occur in the machine impedance characteristic. The parameters R_t , L_t , and C_t are related to the stator winding turn-to-turn capacitance and captures the second-order resonance point. The resistors R_g are added in series with winding to ground capacitors C_g to represent the machine frame resistance. LF transience is partially modelled using the "dq Model" where the LF parameters R and L_d in Fig. 21 (a) can be included. With the addition of the R_t , L_t , and C_t parameters comes an additional level of complexity where determination of these terms requires a "trial-and-error" method.

[53] utilised a single phase HF equivalent circuit as shown in Fig. 22 (b) developed in [54] to model the HF impedance characteristics of 20 different machines, consisting of 14 induction, 4 synchronous reluctance, and 2 brushless, rated between 1.5-55kW. The phase-to-neutral and phase-to-ground impedance was measured from a range of 1kHz to 1MHz using an impedance analyser and the parameters of equivalent circuit were fitted using least square fitting with a "trial-and-error" procedure involving heavier weightings around the first resonance peaks. Each parameter of the HF equivalent circuit for each machine was plotted with respect to machine rated power and trend lines were fitted. The accuracy and time domain simulations of the models are presented in [54] where it can sufficiently model the first resonance point of the phase-to-neutral impedance and the first resonance and anti-resonance point of the phase-to-ground impedance and modelling the phase current and ground current.

[55] proposes a universal high-frequency per-phase machine model suitable for Δ and Y connections as seen in Fig. 23. It extends the proposed model of [51] as shown in Fig. 21 (b) to provide a more accurate representation of the DM and CM impedance characteristics. This model assumes the distributed line of the stator winding can be represented by a series lumped equivalent circuits.

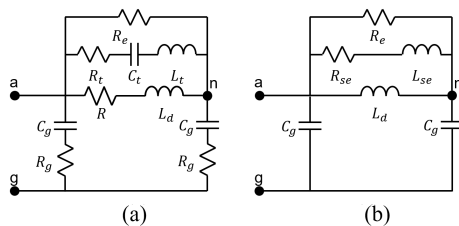


Figure 22: Per-phase high-frequency equivalent circuit from (a) [27], (b) [53].

Similar to the model proposed in [51], the first few turns of the winding is used to model the HF characteristics as HF components of the supply voltage cannot penetrate much further than the first few turns and winding-to-stator stray capacitance of the first few turns is considered a low impedance path in the HF range. This path consists of the resistor R_g representing resistive losses in the CM and DM current path, the stray inductance L_c of the machine terminals and connector wires to winding and winding-to-stator stray capacitances C_{g1} . The centre portion of the winding is used to represent the LF characteristics as LF components of the supply voltage can further penetrate into the winding. This is represented by winding stray inductances L_s and L_{Se} , eddy-current loss resistances R_e and R_{ee} , and the central winding to stator stray capacitance C_{g2} . To make the winding symmetrical so it can be connected in both Y or Δ , the same R_g , L_c , C_{g1} , R_e and L_s are repeated on the opposite side with C_{g2} , L_{Se} , R_{ee} representing the centre LF part of the winding. The lumped parameters C_T , L_T , and R_T represent the inter-turn effects from both ends of the phase winding. The proposed per-phase model of [51] is verified for a 6.5kW BLDC machine. The measured and calculated CM impedance characteristics match well, capturing all significant resonance points up to 10MHz. Minor antiresonance/resonance points at very high frequencies are ignored. Measured and calculated DM impedance characteristics did not match as well as some deviation is observed in the antiresonance point at mid-frequency due to not fully modelling the stray inductance effects of the central part of the winding. In time domain simulations, the simulated CM and DM current responses matched well with the measured response, with the CM current simulation providing better results compared to the DM. Some HF voltage oscillations in the measured response for both CM and DM are not accounted in simulation as HF minor resonances were not modelled.

[56] proposes a universal low-to-high frequency induction machine model as seen in Fig. 24. It takes the IEEE 112 recommended per-phase LF equivalent circuit, marked by the dotted line, and adds parameters to model the HF characteristics of induction machines. The LF portion consists of the LF stator resistance R_s , the stator inductance L_{ls} , the magnetising inductance L_m , the equivalent core-loss resistor R_{core} , the rotor inductance L_{lr} , the rotor resistance R_r and the slip s . The frequency range considered is from 10Hz - 10MHz. To model the resonance and anti-resonance points, three capacitors are used: the

tance, ηL_{ss} is the effective high frequency stator inductance, C_{sf} and R_{sf} are the effective stator-to-frame capacitance and resistances. Similarities between universal per-phase induction model as shown in Fig. 24 and the proposed HF PM model can be seen as both take an existing standard low-frequency induction machine and permanent magnet machine equivalent circuits respectively and add the parameters to capture the mid-to-high frequency characteristics. The models were experimentally validated for a 1.4kW and 5.5kW permanent magnet machine and showed an excellent match for both the DM and CM impedance characteristics up to 10MHz. Discrepancies were observed in the CM and DM mid-frequency resonance because the stator lamination and frame paths are not considered in the DM model. This accounted for with the addition of frame inductance and resistance need to be experimentally determined [58].

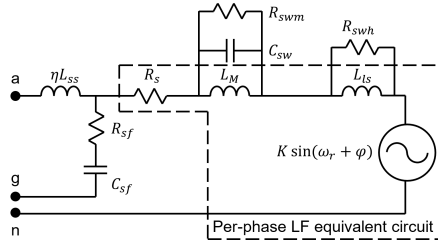


Figure 25: Per-phase low-to-high frequency permanent magnet model. [57]

5.3 Bearing Model

HF CM voltage generated by VSI operation causes a HF CM current. This in turn excites a circumferential HF CM flux around the machine shaft that induces a shaft voltage and circulating bearing current.

NEMA MG1 Standard [59] defines a shaft voltage threshold of 300mV peak for poly-phase squirrel-cage induction machines rated at or less than 3600kW and 7200V. IEC 60034-25 [60] states a limit of 500mV peak for low-voltage machines.

The occurrence of HF electrical discharge in bearings is strongly dependent on the bearing voltage ratio (BVR) as shown,

$$BVR = \frac{v_b}{v_{com}} = \frac{C_{WR}}{C_{WR} + C_{bDE} + C_{RS} + C_{bNDE}}. \quad (36)$$

The parameters representing lumped winding-to-rotor capacitance C_{WR} , rotor-to-stator capacitance C_{RS} and bearing capacitances for the drive-end and non-drive-end C_{bDE} and C_{bNDE} respectively in (36) can be determined analytically as shown in [61] [62], FEM-calculated [62] [63], experimentally measured directly using an LCR meter [64], and determined from machine impedance characteristic measurements [51].

In [61], C_{RS} is determined analytically by considering the stator and rotor as cylindrical capacitors. The winding-to-rotor capacitance for each open slot is

modelled by a series of two parallel-plate capacitors, one representing the airgap, and one representing the upper slot insulation. This value is then multiplied by the number of slots to get the total winding-to-rotor capacitance. Bearing capacitance is determined by considering the capacitance between the bearing and the inner runner surface and the capacitance between the bearing and the outer runner surface. This is determined using the minimum thickness of lubricant on the bearing and the Hertzian contact area [63][65]. The BVR capacitor parameters can be calculated using FEM as seen in [63] where results show good agreement between FEM-calculated and measured BVR values for a 240 kW test induction machine of 3.5% and 3% respectively. BVR is not affected by machine speed, cable length and type (shielded or unshielded). Insulated and hybrid bearings have a minimal effect on BVR. An upper bound BVR of 10% for standard squirrel-cage induction machines is derived from [61] and analytically calculated results for $C_{RS} + C_{WR}$ were up to 15% smaller than measured results.

[66] proposes an equivalent circuit for calculating circulating bearing current i_b and determines a ratio of circulating bearing current to CM current i_{com} , analogous to the BVR as seen in (36). It considers the current distribution in the stator lamination using an eddy-current model. A 2D model with cylindrical symmetry is assumed to determine CM flux from which the impedances along the bearing current path can be derived from. From the analysis, a theoretical maximum ratio for i_b/i_{com} of 0.354 is derived in [66] and are comparable with measured results in [67].

[51] proposes a CM equivalent circuit model for calculating the bearing voltage as seen in Fig. 26. It extends upon the model shown in Fig. 21 (b) with the addition of HF machine capacitances. From the machine terminals' perspective, current can flow to the frame (considered ground) in two different ways, either from the winding to the stator and then to the frame or from the winding to the rotor, through the bearing, then to the stator and finally to the frame. These paths can be modelled with the parasitic elements C_{WR1} and C_{WR2} representing the winding-to-rotor capacitance, C_{g1} and C_{g2} for the distributed winding-to-ground capacitance, C_{RS} for the rotor-to-stator capacitance, and C_{bDE} and C_{bNDE} for the bearing drive-end and non-drive-end capacitances respectively. R_g represents losses in the lamination and frame caused by the CM current flowing to ground. The winding-to-rotor capacitance is split into C_{WR1} and C_{WR2} for the same reason as the winding-to-stator capacitance is split into C_{g1} and C_{g2} where C_{WR1} and C_{g1} considers the HF impedance characteristics of the first few turns. The proposed bearing model in Fig. 26 is verified using 1.5kW and 240kW induction machine by applying switched voltages, measuring the bearing voltage and comparing it with the simulated value. The initial values for C_{WR1} and C_{WR2} lead to inaccurate results for simulated v_b . C_{WR1} and C_{WR2} are adjusted and perfect fitting of the simulated v_b is achieved though the method of how the parameter adjustment is made is not stated in [51].

[55] proposes a CM per-phase equivalent circuit for modelling bearing voltages as seen in Fig. 27. It simplifies the per-phase universal induction machine model as seen in Fig. 23 by elimination of the parameters L_{se} , R_{ee} , R_T , C_T ,

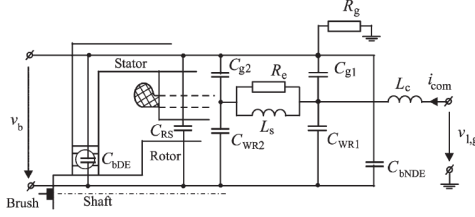


Figure 26: Proposed common-mode equivalent circuit machine model for calculating bearing voltage. [51]

and L_T that are associated with the DM impedance and adding the bearing model. The winding-to-rotor capacitance is distributed across C_{WR1} , C_{WR2} in the same manner C_{g1} and C_{g2} are. The branches contain switches in series with R_{bDE} , L_{bDE} and R_{bNDE} , L_{bNDE} , are connected in parallel with the capacitors C_{bDE} and C_{bNDE} , and are used to simulate the discharge current. R_{bDE} , L_{bDE} , R_{bNDE} , and L_{bNDE} are estimated to get a good match between simulated and measured parameters. Simulated results showed good agreement with measured values, with voltage offset present due to ratio deviation of the winding-to-rotor capacitance and capacitances C_{RS} , C_{bDE} , and C_{bNDE} .

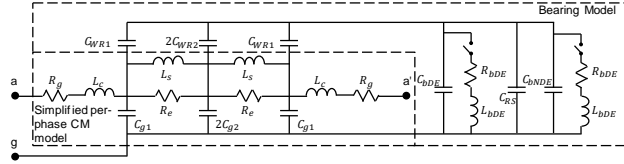


Figure 27: Proposed common-mode equivalent circuit machine model for calculating bearing voltage. [55]

5.4 High Frequency FEA of Machines

HF FEA can be used to determine parameters of the distributed networks to model multi-turn windings and for HF lumped equivalent circuit machine models. Special considerations need to be made when modelling the HF machine characteristics. Skin, proximity and eddy effects, capacitive impedance paths in the machine become more prevalent at higher frequencies. For example, [68] highlighted recommended extensions to the standard transmission line model for HF effects in machine windings and how they can effect the CM and DM impedance characteristics with the inclusion of the complex CM current path through the lamination core, addition of inductive terms from the winding overhang model and considering the inter-wire capacitive and inductive coupling. In

this section, different HF FEA techniques to analyse electrical machines are discussed.

[69] and [70] determined a HF PMSM model using FEA by considering one-pole multi-slot geometry. Conventionally, the slot barrier is assumed to be act as flux barrier at high frequency [71] [72] however [73] showed the potential of inter-slot inductance coupling, even at higher frequencies. Skin effect, proximity effect, and eddy currents are considered when calculating the machine winding's resistance and inductance. Resistance can increase drastically at high frequency while inductance tends to reduce with increase of frequency. To determine resistance and inductance, the 2D Maxwell magnetodynamic time harmonic problem is solved. Because one pole geometry is modelled, the eddy currents in the core, iron losses and inter-slot inductance coupling are accounted for. The mesh size around the turns need to be adjusted such that it should be smaller than the wavelength of the PWM excitation frequency.

[74] propose a low mesh resolution HF approximation FE stator winding machine model. To reduce computational requirement and mesh resolution while getting accurate results, approximations were made where the conductors are assumed to act like flux barriers at HF. As frequency increases, current tends to flow on the outside of a conductor due to the skin effect and thus no flux is present in the centre of a conductor. This eliminates the need for a fine mesh near the outer perimeter of a conductor to accurately model eddy current effects in mid to high frequencies. Results show a good match for the low resolution HF model and the high resolution mid-frequency stator winding model that explicitly considers eddy current, flux and current distribution in the conductors.

[75] developed a HF model of an interior permanent magnet synchronous machine (IPMSM) using FEA of the entire stator and rotor geometry. Unlike an induction machine or surface mounted permanent magnet synchronous machine, the low to mid frequency DM impedance characteristic varies with rotor position due to saliency while in the HF range, it is independent of rotor position and only dependent on stator characteristics as shown in Fig. 28 (a). This corresponds with the experimental observations and conclusions made by [76] as shown in Fig. 28 (b) where the DM impedance characteristics for an induction machine with and without its rotor were compared. The low- to mid-frequency impedance characteristics do not match but the high-frequency impedance above the first resonance point does. Analysis and measurements have shown that CM impedance characteristic does not vary with rotor position for the entire frequency range.

[77] approximates the explicit representation of conductor locations in a slot using a continuum representation known as the foil approach [78] to determine resistances and inductances in 2D FEA while considering the skin and proximity effect. Resistance and inductance variation with frequency is modelled in the equivalent RLC distributed network by replacing the per-turn resistance and inductance with a higher-order RL ladder circuit. Eddy current losses in the iron is represented by a per-turn eddy current resistor. The overhang inductance is also considered, is assumed constant and is included in the distributed network

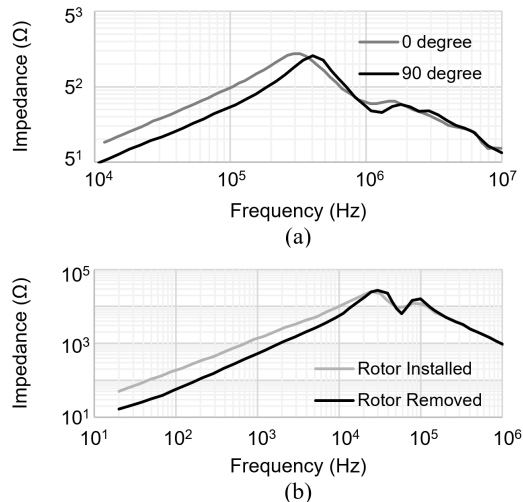


Figure 28: Permanent magnet machine's differential impedance (a) FEA determined IPMSM impedance for different rotor positions[75], (b) Measured impedance with and without rotor installed from [76]

with the addition of a per-turn overhang inductor term.

[73] and [79] model the eddy current effects, common-mode current path and distribution in core laminations using FEA to determine the CM impedance of the machine. The CM impedance path consists of the stator, rotor and overhang. All the laminations in an entire machine cannot be modelled explicitly due the enormous number of elements and computation requirements. In [73], half of the lamination sheet with half an oxide layer is modelled instead whereas [79] models a single lamination in both 2D [80] and 3D FEA. Periodic boundary conditions are applied on the faces of the lamination side and the model is discretised using prismatic elements to reduce the degrees of freedom by taking advantage of the laminations symmetry.

[81] used FEA to predict the potential partial discharge inception voltage in a machine coil. The electrostatic potential and electric field lines in the coil derived from FEA, as shown in Fig. 29, are compared with the breakdown voltages derived from the Paschen's curve for a given pressure and separation distance. This is done by solving the electric field intensity E -oriented scalar formulation and electric displacement flux density D -oriented formulation,

$$E = -\nabla V, \quad (37)$$

$$D = \nabla \times u, \quad (38)$$

where V is the electric scalar potential and u is the vector potential.

[82] and [83] used FEA to determine the maximum turn-to-turn voltage in a mush wound machine by considering the position of each turn in a slot. The

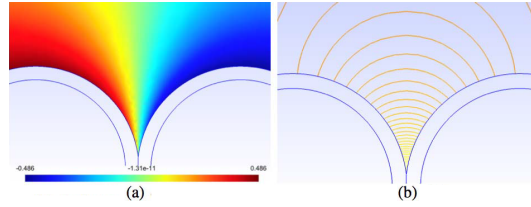


Figure 29: Electrostatic and electric field potential results of machine coil [81]. (a) Scalar potential distribution. (b) Electric field lines.

optimal arrangement of the turns in a slot can be determined to minimise this turn-to-turn voltage. From [82]’s comparison of different conductor arrangements, it concluded that successive turns should be placed next to each other to minimise turn-to-turn voltage. The worst case arrangement is when the last turn is placed next to the first turn as the first turn experiences the full incoming step voltage and the last turn can remain at ground until the voltage wave propagates through all of the turns.

[84] describes a method of calculating the end winding reactance using 3D FEA. This consists of determining the stored magnetic energy from computing the 3D flux density distribution when the machine is supplied by a three phase source. Because it is difficult to isolate the end windings from the rest of the stator, the rotor is removed and the total stator reactance is computed for various stack lengths. Reactance is plotted against stator length and extrapolated to where stack length is equal to zero to find the reactance that corresponds to the end winding. [85] and [86] provide a 3D analytical approach to calculate the end winding inductance based on the Neumann’s integral solution. The proposed method combines with the method of mirror images such that stator and rotor magnetic effects are accounted for. [85] validated the analytical method against 3D FEA model, showing a 2% discrepancy between 3D FEA and analytically calculated values for 16.2MVA round-rotor synchronous machine.

6 Inverter

In the previous sections, it can be seen that the analysing, modelling, and simulation of motor drives with respect to the cables and motor has been thoroughly investigated. However, comparatively little research into the effects of long cable feeders cables on inverter operation and switching characteristics has been found. Here, the effects of long cable loading on inverter switching characteristics are introduced and inverter operation considerations are described.

oscillations' peak is 24A ($3 \times$ that of nominal) and goes negative for 100ns, desaturating the IGBT. The total switching energy increases up by 33.3% when comparing 2m to 50m.

The transient IGBT turn-off voltage for different cable lengths is shown in Fig. 32 (b). Voltage rise increases with cable length and cable parasitic capacitance. A plateau can be observed for both the 24m and the 50m cable during the rise time period. The duration of the plateau corresponds directly to charging time of cable capacitance and is double that of cable's wave propagation time. For the 50m cable case, the propagation time was determined to be 0.54 μ s from the inductance and capacitance per unit length of cable.

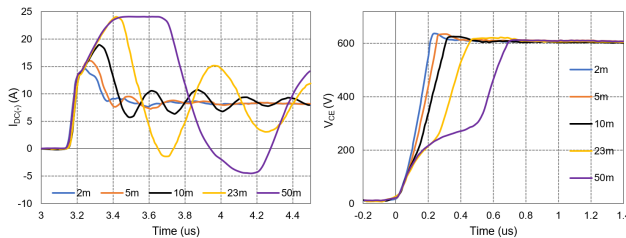


Figure 32: Switching characteristics for different cable lengths (a) Collector turn-on current. (b) Emitter-collector turn-off voltage. [87]

A comparison between shielded and non-shielded cables was made. Due to the absence of the cable's shield, the parasitic capacitance between phase and ground is reduced which in turn leads to a reduction in the turn-on current and turn-on energy and faster turn-off. However, it is acknowledged that a shield may be required during for electromagnetic compatibility and inference.

6.2 Inverter operation considerations with long cable loading

For higher current ratings, these additional switching losses become less significant as they take up a smaller proportion of total switching losses. Semiconductor switching losses scale linearly with respect to nominal operating current (10A to 100A IGBT correlates to approximately a factor of 10 increase in semiconductor switching losses), while cable capacitance rises by less than factor of 3 of that of the nominal current capability.

Interlock times and short circuit detection blanking times need to be adjusted to prevent a short circuit between the switches of one inverter leg. Data sheet values for delay, rise, and fall time can no longer be used to determine this interlock time as it is dependent in this case on the cable's parasitic capacitances. IGBT short circuit detection is done by measuring $V_{ce(sat)}$ during saturation. If this value is measured when it exceeds the reference value during high transient collector current oscillation turn-on period, it cause the drive to set to failure mode, switching the IGBT off. Conventionally, the measurement is delayed

by the blanking time after the turn-on command to allow for any transient oscillations to dissipate.

Turn-off rise times are further increased while turn-on current oscillations amplitude reduced with lower operating load current leads to slower charging of the parasitic capacitance as seen in Fig. 33 [89]. The machine operation mode and duty cycle needs to be considered for full cycle power loss, efficiency calculations and correct adjustment of interlock and blanking times.

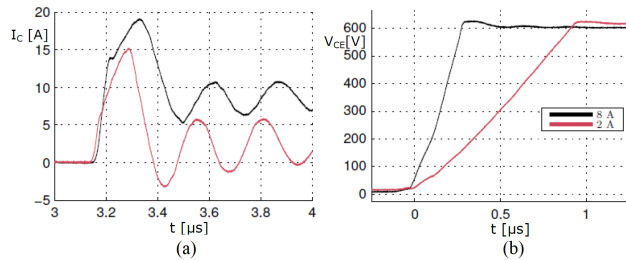


Figure 33: Switching characteristics for different loading currents. (a) Collector turn-on current. (b) Emitter-collector turn-off voltage. [89]

Higher inverter switching frequency and certain modulation schemes with long feeder cables can lead to voltage oscillations of amplitude greater than twice that of the DC bus voltage. Fig. 34 shows the condition where voltage oscillations have not sufficiently decayed before another step change in voltage was applied on the inverter end. Voltage oscillation frequency and rate of damping increases with the reduction of cable length thus phenomenon is more apparent with systems with longer feeder cables, shorter pulse widths and higher switching frequency. [13] proposed an active pulse elimination technique (PET) which modifies the PWM algorithm to prevent double pulsing and polarity reversals. The technique was validated for the operating condition of 60Hz, no load, 8kHz carrier and 650Vdc bus. Fig 35 shows the machine side per unit voltage for different lengths of cable, with and without PET correction. Voltages with PET correction were maintained within that of the inverter-grade machine ratings.

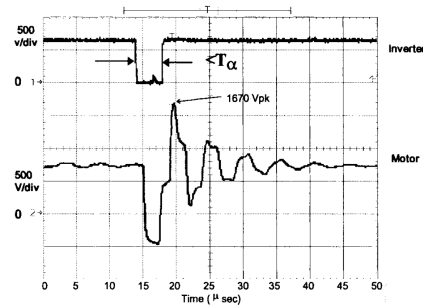


Figure 34: Greater than 2pu machine side voltage due double pulsing. [13]

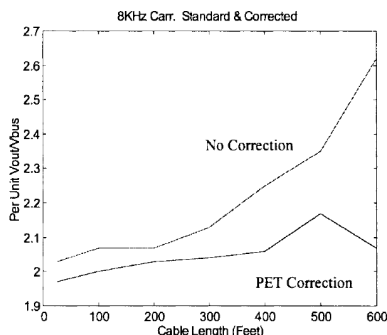


Figure 35: Machine side voltage for different cable lengths with and without pulse elimination technique correction. [13]

7 Mitigation Methods

In this section, different methods to mitigate voltage oscillations caused by fast-switching inverters and poor machine-cable surge-impedance mismatch are discussed. Extensive studies have been made on the RL/RC/LC/RLC inverter filters in different arrangements for mitigation of over-voltage in machine-drive systems with long feeder cables [91] [92] [93] [94], some which have been compared in [95] [96]. These schemes would be discussed in lesser detail as the presented mitigation schemes are comparatively novel, smaller, and/or have lower losses.

Filtering solutions to mitigate over-voltage caused by transmission line effects generally fall into one of these categories, sine-wave filters, dv/dt filters, and impedance matching.

Sine-wave filter's cut-off frequency is between that of the fundamental frequency of the machine and the switching frequency of the inverter. As sinusoidal voltages are applied, sinusoidal voltages are seen on the machine side as well which in turn reduce voltage oscillations, inter-turn voltage reflections in the machine windings. This also reduces the potential for high bearing currents as the machine side common-mode voltage at any time is low. The switching characteristics are filtered out and smooth voltages with intrinsically low dv/dt are applied to the cable's inverter side to mitigate machine side voltage overshoot. The difficulty with filter design is mitigation of its intrinsic resonance and the filter's cut-off frequency is selected such that it doesn't interact with either the fundamental or switching frequencies. The use of a resistance can dampen these resonance and can lead to increase in filter losses.

The dv/dt filter's cut-off frequency is typically above the switching frequency of the inverter. It reduces the steepness of switched voltage front, thus reducing the peak side voltage overshoot. Because the cut-off frequency of the filter is above that of the inverter's switching frequency, the associated passives would be smaller, lighter, and have lower losses. However, because the switching characteristics are not filtered, this may cause issues with EMI and filter resonance with the switching fundamental and side band harmonics.

Impedance matching involves the addition of components on the load side such that the load side's impedance matches that of the characteristic impedance of the feeder cable. [92] and [97] utilised a star connected RC circuit in parallel with the terminals of the machine. The capacitor acts as a high frequency short-circuit at the instance of voltage step occurring and acts as an open circuit during at DC, and the resistor is selected such that load side's surge impedance matches that of the cable's at voltage step transience. However, the use of resistors in the impedance matching increased losses. In [97], the designed load side RC filter's losses are 45W for 4.5kW machine operating at 208V line-to-line and 230W at 460V line-to-line.

[93] provides an equation for peak load side line to line voltage $V_{LL,p}$ as a function of inverter rise time t_r with a given cable of propagation time t_p , machine with load side reflection coefficient Γ_L , DC bus source voltage V_{DC} , and velocity of propagation v_p ,

$$V_{LL,p} = \frac{3l_c V_{DC} \Gamma_L}{v_p t_r} + V_{DC}, \text{ for } t_p < \frac{t_r}{3}, \quad (39)$$

$$V_{LL,p} = V_{DC} \Gamma_L + V_{DC}, \text{ for } t_p \geq \frac{t_r}{3}. \quad (40)$$

It can be seen for propagation times greater or equal to a third of the inverter rise time, the peak load side line to line voltage is independent of rise time. Thus, over voltage mitigation can be achieved with increase of the source side applied voltage or reduction in the cable length and thus propagation time.

Correct pairing of the cable and machine considering their respective impedance characteristics is essential. Inverter side passive and active output filters can ensure non-steep fundamental sinusoidal-like voltages are applied on the cable's inverter side. [8] describes the failure mode of stator windings due to the anti-resonance nodes of cable's and machine's impedance characteristics. The study was motivated by stator winding faults in a series of 460V 300hp induction machines and varying lengths of feeder cables. It was observed that machines with the relatively long cable lengths did not fail while the machines with short lengths did. The measured line-to-ground impedance for the different cables and machines are compared and it was found that the anti-resonance point of the relatively short cable is similar to that of the machine and this is the cause of the failure. The recommended solution is to swap the machine or cable such that the impedance anti-resonance point for each device are not at similar frequencies or use an inverter output filter.

[2] demonstrates a low-loss "RL-plus-C" filter to mitigate over-voltage associated with drive systems and long feeder cable. The filter consists of an RL parallel branch connected in-line with the inverter output and the capacitor connected line-to-line on the load side as shown in Fig. 36. The power loss of the proposed filter is compared against the conventional RC and RLC filters. The test system consists of a 1hp induction machine with a 100m cable feeder. For a design target of 3.3% machine side voltage overshoot, the proposed filter's power loss is 36W while RLC and RC consumed 335W and 275W respectively.

[98] provided additional passive filter variations, named "RLC_{CM}-plus-C" and "RLC_{CM}" and compared them to the "RL-plus-C" filter for power loss and CM current mitigation. Out of the three filters, "RL-plus-C" filter had the lowest power loss and "RLC_{CM}" is the best at mitigating CM current, and thus bearing current.

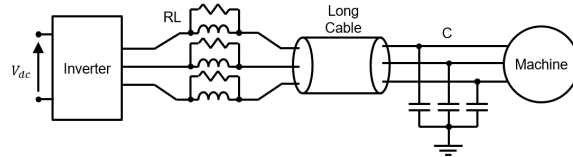


Figure 36: "RL-Plus-C" filter. [2]

The use of inverter active output filters (AOF) to generate a sinusoidal output voltage is described in [99] and [100] as shown in Fig. 37. For AOF the passive LC output filter is replaced with a fast switching H-bridge stage and LC output stage. Because the H-bridge is switching at a much higher frequency, the LC output stage can be smaller. [99] compared the performance, size and losses between an AOF and a passive LC filter for 156kVA 400Hz variable speed constant frequency aerospace power system where both filters were sized for the same target current ripple and cut-off frequency. A size reduction of 91% is achieved for the AOF design with the main VSCF inverter and H-bridge switching at 5kHz and 50kHz respectively compared to the passive LC filter solution at 10kHz switching. [100] showed AOF can more effectively filter out the main inverter fundamental switching frequency and low order switching frequency side-bands from the output compared to a passive LC filter when designed for the same current ripple and cut-off frequency.

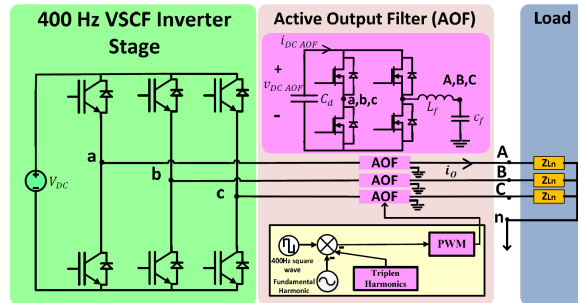


Figure 37: Active output filter. [99]

[101] investigated using an over-voltage mitigation method using three-level inverter as seen in Fig. 38. The voltage is stepped from DC-, to mid-point, and then to DC+. A dwell time t_{dw} equal to twice the propagation delay is introduced between the first and second applied voltage step. The effect of this switching scheme is the voltage oscillations caused by the first switching incident

is cancelled by the oscillations caused by the second delayed switching incident.

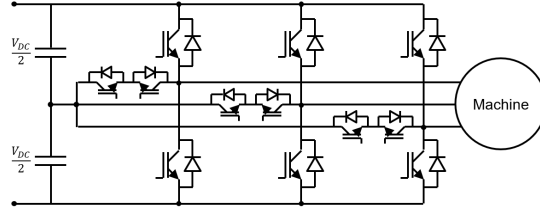


Figure 38: Three-level inverter. [101]

This switching technique was experimentally validated on a drive system with 50A/600V IGBTs, 100m 2.0mm² PVC cable, and 2.2kW induction machine. The measured inverter and machine voltages with and without the dwell time delay applied can be seen in Fig. 39. Clear attenuation of machine side over voltage can be seen when comparing Fig. 39 (c) and (d). The advantage of this technique is its absence of the passive filter components, leading to reduction in mass and volume of entire drive system.

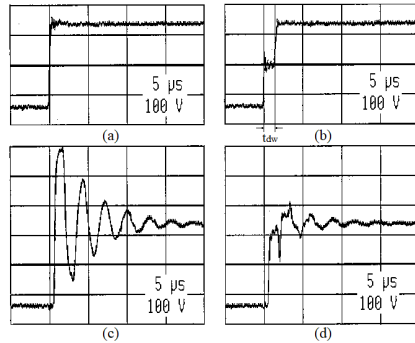


Figure 39: Scope measurement for inverter and machine voltages of three-level inverter (a) Inverter voltage without dwell time. (b) Inverter voltage with dwell time. (c) Machine voltage without inverter dwell time. (d) Machine voltage with inverter dwell time. [101]

[102] and [103] investigated the use of an LC inverter output filter with diode bridge topology. The LC clamp filter reduces the dV/dt of the switched voltages applied to the inverter side of the long feeder cable, thus reducing the machine side over voltage. The diode bridge ensures the resonant voltage on the cable's source side and LC filter output does not exceed the sum voltage of the DC link and the voltage across the snubber circuit as shown in Fig. 40. Absence of the diode bridge can cause undamped resonance to occur in the output of the LC filter. The cable's source sides voltage's dv/dt is determined by the

cut-off frequency of the LC filter which can be set above that of the switching frequency. The advantage of this is much smaller components and lower losses compared to conventional sin-wave filters.

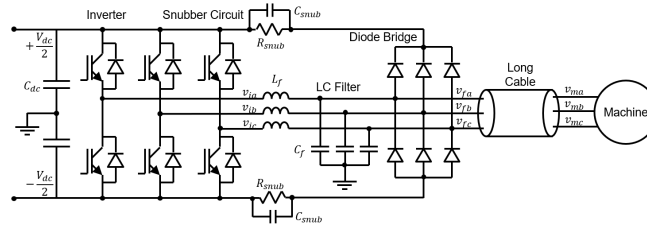


Figure 40: LC filter with diode bridge dv/dt filter. [103]

8 Conclusion

A literature review on electric drive systems with long feeder cables has been presented. Steep-fronted switched voltages and poor machine-cable impedance matching can lead to high-amplitude and high-frequency voltage oscillations throughout the cable and machine due to transmission line effects. This can cause EMI, corona discharge, high CM and DM currents and bearing currents. To analyse these voltage oscillations, high frequency cable and machine models are required and presented in this review. Both the models and methods of how to acquire the parameters through measurement, analytical techniques, and FEA are presented. The effects of capacitive cable loading on inverter switching characteristics have been outlined. Mitigation methods of high-amplitude high-frequency voltage oscillations using sine-wave, dv/dt filters, active out filters, different filtering topologies are shown with a particular focus on novel, small size, and/or low-loss solutions. Reducing these voltage oscillations also eliminate or reduce the effect of all of the problems associated with it.

References

- [1] O. V. Thorsen and M. Dalva, "A survey of faults on induction motors in offshore oil industry, petrochemical industry, gas terminals and oil refineries," in *Petroleum and Chemical Industry Conference, 1994. Record of Conference Papers., Institute of Electrical and Electronics Engineers Incorporated Industry Applications Society 41st Annual*, pp. 1–9, Sep 1994.
- [2] K. K. F. Yuen and H. S. H. Chung, "A low-loss RL-Plus-C filter for over-voltage suppression in inverter-fed drive system with long motor cable," *IEEE Transactions on Power Electronics*, vol. 30, pp. 2167–2181, April 2015.

- [3] I. Christou, A. Nelms, I. Cotton, and M. Husband, “Choice of optimal voltage for more electric aircraft wiring systems,” *IET Electrical Systems in Transportation*, vol. 1, pp. 24–30, March 2011.
- [4] M. Fenger, S. R. Campbell, and J. Pedersen, “Dealing with motor winding problems caused by inverter drives,” in *IEEE-IAS/PCS 2002 Cement Industry Technical Conference. Conference Record (Cat. No.02CH37282)*, pp. 65–76, 2002.
- [5] A. Lima, R. Stephan, and A. Pedroso, “Modelling the electrical drive system for oil exploitation,” in *International Power System Transients Conference*, pp. 234–239, 1997.
- [6] V. C. de Paula and H. de Paula, “Employing DC transmission in long distance ac motor drives: Analysis of the copper economy and power losses reduction in mining facilities,” in *2015 IEEE Industry Applications Society Annual Meeting*, pp. 1–7, Oct 2015.
- [7] M. Bendjedia, A. Khlaief, and M. Boussak, “Sensorless speed control of outrunner PMSM drive connected to long cable for flying remote operative vehicle,” in *2012 XXth International Conference on Electrical Machines*, pp. 2252–2258, Sept 2012.
- [8] B. Mirafzal, G. L. Skibinski, and R. M. Tallam, “A failure mode for PWM inverter-fed AC motors due to the antiresonance phenomenon,” *IEEE Transactions on Industry Applications*, vol. 45, pp. 1697–1705, Sept 2009.
- [9] A. C. S. de Lima, R. M. Stephan, A. Pedroso, and J. Mourente, “Analysis of a long distance drive for an induction motor,” in *Proceedings of IEEE International Symposium on Industrial Electronics*, vol. 2, pp. 867–872 vol.2, Jun 1996.
- [10] B. Sarlioglu and C. T. Morris, “More electric aircraft: Review, challenges, and opportunities for commercial transport aircraft,” *IEEE Transactions on Transportation Electrification*, vol. 1, pp. 54–64, June 2015.
- [11] J. Li, Z. Yu, Y. Huang, and Z. Li, “A review of electromechanical actuation system for more electric aircraft,” in *2016 IEEE International Conference on Aircraft Utility Systems (AUS)*, pp. 490–497, Oct 2016.
- [12] P. Janker, F. Claeysen, B. Grohmann, M. Christmann, T. Lorkowski, R. LeLetty, O. Sosniki, and A. Pages, “New actuators for aircraft and space applications,” in *Proc Actuator*, pp. 325–330, 2006.
- [13] R. Kerkman, D. Leggate, and G. Skibinski, “Interaction of drive modulation and cable parameters on AC motor transients,” in *Industry Applications Conference, 1996. Thirty-First IAS Annual Meeting, IAS '96., Conference Record of the 1996 IEEE*, vol. 1, pp. 143–152 vol.1, Oct 1996.

- [14] T. Billard, T. Lebey, and F. Fresnet, "Partial discharge in electric motor fed by a PWM inverter: off-line and on-line detection," *IEEE Transactions on Dielectrics and Electrical Insulation*, vol. 21, pp. 1235–1242, June 2014.
- [15] R. S. Arajo, R. A. Rodrigues, H. de Paula, B. J. C. Filho, L. M. R. Baccharini, and A. V. Rocha, "Premature wear and recurring bearing failures in an inverter driven induction motor 2014; part II: The proposed solution," in *2013 IEEE Industry Applications Society Annual Meeting*, pp. 1–8, Oct 2013.
- [16] F. W. Peek, *Dielectric phenomena in high-voltage engineering*. 1929.
- [17] H. Southall, "High voltage design guide for airborne equipment," *AD-A029*, vol. 268.
- [18] E. Sili, F. Koliatene, and J. P. Cambronne, "Pressure and temperature effects on the Paschen curve," in *2011 Annual Report Conference on Electrical Insulation and Dielectric Phenomena*, pp. 464–467, Oct 2011.
- [19] EASA, "The effect of repair/rewinding on motor efficiency. technical report," 2003.
- [20] W. Tong, *Mechanical design of electric motors*. CRC press, 2014.
- [21] T. Hadden, J. W. Jiang, B. Bilgin, Y. Yang, A. Sathyan, H. Dadkhah, and A. Emadi, "A review of shaft voltages and bearing currents in EV and HEV motors," in *IECON 2016 - 42nd Annual Conference of the IEEE Industrial Electronics Society*, pp. 1578–1583, Oct 2016.
- [22] R. S. Arajo, R. A. Rodrigues, H. de Paula, L. M. R. Baccharini, and A. V. Rocha, "Premature wear and recurring bearing failures in an inverter driven induction motor 2014; part I: Investigation of the problem," in *2013 IEEE Industry Applications Society Annual Meeting*, pp. 1–6, Oct 2013.
- [23] Department of Defense United States of America, "MIL-STD-461G," Dec 2015.
- [24] US Navy, "Aircraft electric power characteristics," tech. rep., MIL-STD-704F, 2004.
- [25] Radio Technical Commission for Aeronautics, "RTCA/DO-160 G Change 1F," Dec 2014.
- [26] A. Hoshmeh, K. Malekian, W. Schufft, and U. Schmidt, "A single-phase cable model based on lumped-parameters for transient calculations in the time domain," in *2015 IEEE 15th International Conference on Environment and Electrical Engineering (EEEIC)*, pp. 731–736, June 2015.

- [27] A. F. Moreira, T. A. Lipo, G. Venkataramanan, and S. Bernet, "High-frequency modeling for cable and induction motor overvoltage studies in long cable drives," *IEEE Transactions on Industry Applications*, vol. 38, pp. 1297–1306, Sep 2002.
- [28] L. Wang, C. N.-M. Ho, F. Canales, and J. Jatskevich, "High-frequency modeling of the long-cable-fed induction motor drive system using TLM approach for predicting overvoltage transients," *IEEE Transactions on Power Electronics*, vol. 25, pp. 2653–2664, Oct 2010.
- [29] S. H. Hall, G. W. Hall, J. A. McCall, *et al.*, *High-speed digital system design: a handbook of interconnect theory and design practices*. Citeseer, 2000.
- [30] R. C. da Silva, S. Kurokawa, *et al.*, "Model of three-phase transmission line with the theory of modal decomposition implied," *Energy and Power Engineering*, vol. 5, no. 04, p. 1139, 2013.
- [31] B. Gustavsen and A. Semlyen, "Rational approximation of frequency domain responses by vector fitting," *IEEE Transactions on Power Delivery*, vol. 14, pp. 1052–1061, Jul 1999.
- [32] B. Gustavsen, "Improving the pole relocating properties of vector fitting," *IEEE Transactions on Power Delivery*, vol. 21, pp. 1587–1592, July 2006.
- [33] E. C. M. Costa, S. Kurokawa, J. Pissolato, and A. J. Prado, "Efficient procedure to evaluate electromagnetic transients on three-phase transmission lines," *IET Generation, Transmission Distribution*, vol. 4, pp. 1069–1081, September 2010.
- [34] A. Hoshmeh, "A three-phase cable model based on lumped parameters for transient calculations in the time domain," in *2016 IEEE Innovative Smart Grid Technologies - Asia (ISGT-Asia)*, pp. 580–585, Nov 2016.
- [35] T. Ming, S. Jianyang, G. Jianzhao, L. Hongjie, Z. Wei, and L. Deliang, "Time-domain modeling and simulation of partial discharge on medium-voltage cables by vector fitting method," *IEEE Transactions on Magnetics*, vol. 50, pp. 993–996, Feb 2014.
- [36] C. Purcarea, P. Mutschler, O. Magdun, A. Rocks, and A. Binder, "Time domain simulation models for inverter-cable-motor systems in electrical drives," in *2009 13th European Conference on Power Electronics and Applications*, pp. 1–10, Sept 2009.
- [37] C. Purcarea, *High-frequency parasitic effects in electric drives with long cables*. PhD thesis, Technische Universität, 2011.
- [38] N. Idir, Y. Weens, and J. J. Franchaud, "Skin effect and dielectric loss models of power cables," *IEEE Transactions on Dielectrics and Electrical Insulation*, vol. 16, pp. 147–154, February 2009.

- [39] G. Skibinski, R. Tallam, R. Reese, B. Buchholz, and R. Lukaszewski, “Common mode and differential mode analysis of three phase cables for PWM AC drives,” in *Conference Record of the 2006 IEEE Industry Applications Conference Forty-First IAS Annual Meeting*, vol. 2, pp. 880–888, Oct 2006.
- [40] F. Piriou and A. Razek, “Finite element analysis in electromagnetic systems-accounting for electric circuits,” *IEEE Transactions on Magnetics*, vol. 29, pp. 1669–1675, Mar 1993.
- [41] A. W. Cirino, H. de Paula, R. C. Mesquita, and E. Saraiva, “Cable parameter variation due to skin and proximity effects: Determination by means of finite element analysis,” in *2009 35th Annual Conference of IEEE Industrial Electronics*, pp. 4073–4079, Nov 2009.
- [42] M. Hichem, D. Nizar, B. Adel, and H. A. Hsan, “Modeling of an underground cable fled in two-layer soil,” in *2014 First International Conference on Green Energy ICGE 2014*, pp. 144–151, March 2014.
- [43] M. Diaz-Aguil, F. D. Len, S. Jazebi, and M. Terracciano, “Ladder-type soil model for dynamic thermal rating of underground power cables,” *IEEE Power and Energy Technology Systems Journal*, vol. 1, pp. 21–30, Dec 2014.
- [44] N. Y. Abed and O. A. Mohammed, “Frequency-dependent coupled field-circuit modeling of armored power cables using finite elements,” *IEEE Transactions on Magnetics*, vol. 47, pp. 930–933, May 2011.
- [45] L. Gubbala, A. von Jouanne, P. Enjeti, C. Singh, and H. Toliyat, “Voltage distribution in the windings of an AC motor subjected to high dv/dt PWM voltages,” in *Power Electronics Specialists Conference, 1995. PESC '95 Record., 26th Annual IEEE*, vol. 1, pp. 579–585 vol.1, Jun 1995.
- [46] Y. Tang, “Analysis of steep-fronted voltage distribution and turn insulation failure in inverter fed AC motor,” in *Industry Applications Conference, 1997. Thirty-Second IAS Annual Meeting, IAS '97., Conference Record of the 1997 IEEE*, vol. 1, pp. 509–516 vol.1, Oct 1997.
- [47] A. Abbasi and J. Nazarzadeh, “A traveling-wave model of electric machines with eccentricity for shaft voltage analysis,” *Journal of Electromagnetic Waves and Applications*, vol. 28, no. 18, pp. 2290–2307, 2014.
- [48] I. Rasoanarivo, C. Tyrel, N. Takorabet, and F. M. Sargos, “High frequency modeling of the winding wires of AC machines,” in *2013 15th European Conference on Power Electronics and Applications (EPE)*, pp. 1–12, Sept 2013.
- [49] G. Lupo, C. Petrarca, M. Vitelli, and V. Tucci, “Multiconductor transmission line analysis of steep-front surges in machine windings,” *IEEE*

Transactions on Dielectrics and Electrical Insulation, vol. 9, pp. 467–478, Jun 2002.

- [50] M. T. Wright, S. J. Yang, and K. McLeay, “General theory of fast-fronted interturn voltage distribution in electrical machine windings,” *IEE Proceedings B - Electric Power Applications*, vol. 130, pp. 245–256, July 1983.
- [51] O. Magdun and A. Binder, “High-frequency induction machine modeling for common mode current and bearing voltage calculation,” *IEEE Transactions on Industry Applications*, vol. 50, pp. 1780–1790, May 2014.
- [52] A. Boglietti and E. Carpaneto, “Induction motor high frequency model,” in *Conference Record of the 1999 IEEE Industry Applications Conference. Thirty-Forth IAS Annual Meeting (Cat. No.99CH36370)*, vol. 3, pp. 1551–1558 vol.3, 1999.
- [53] A. Boglietti, A. Cavagnino, and M. Lazzari, “Experimental high-frequency parameter identification of ac electrical motors,” *IEEE Transactions on Industry Applications*, vol. 43, pp. 23–29, Jan 2007.
- [54] E. Carpaneto, A Boglietti, “An accurate induction motor high-frequency model for electromagnetic compatibility analysis,” *Electric Power Components and Systems*, vol. 29, no. 3, pp. 191–209, 2001.
- [55] G. Vidmar and D. Miljavec, “A universal high-frequency three-phase electric-motor model suitable for the delta- and star-winding connections,” *IEEE Transactions on Power Electronics*, vol. 30, pp. 4365–4376, Aug 2015.
- [56] B. Mirafzal, G. L. Skibinski, R. M. Tallam, D. W. Schlegel, and R. A. Lukaszewski, “Universal induction motor model with low-to-high frequency-response characteristics,” *IEEE Transactions on Industry Applications*, vol. 43, pp. 1233–1246, Sept 2007.
- [57] M. A. Gries and B. Mirafzal, “Permanent magnet motor-drive frequency response characterization for transient phenomena and conducted emi analysis,” in *2008 Twenty-Third Annual IEEE Applied Power Electronics Conference and Exposition*, pp. 1767–1775, Feb 2008.
- [58] B. Mirafzal, G. L. Skibinski, and R. M. Tallam, “Determination of parameters in the universal induction motor model,” in *2007 IEEE Industry Applications Annual Meeting*, pp. 1207–1216, Sep. 2007.
- [59] National Electrical Manufacturers Association, *Standard NEMA MG-1-1998: Motors and Generators*. Standard - National Electric Manufacturers Association, National Electrical Manufacturers Association, 2000.
- [60] “IEEE Standard Test Procedure for Polyphase Induction Motors and Generators,” *IEEE Std 112-2004 (Revision of IEEE Std 112-1996)*, 2004.

- [61] A. Muetze and A. Binder, "Calculation of motor capacitances for prediction of the voltage across the bearings in machines of inverter-based drive systems," *IEEE Transactions on Industry Applications*, vol. 43, pp. 665–672, May 2007.
- [62] O. Magdun, Y. Gemeinder, and A. Binder, "Prevention of harmful EDM currents in inverter-fed AC machines by use of electrostatic shields in the stator winding overhang," in *IECON 2010 - 36th Annual Conference on IEEE Industrial Electronics Society*, pp. 962–967, Nov 2010.
- [63] O. Magdun and A. Binder, "Calculation of roller and ball bearing capacitances and prediction of edm currents," in *2009 35th Annual Conference of IEEE Industrial Electronics*, pp. 1051–1056, Nov 2009.
- [64] D. Busse, J. Erdman, R. J. Kerkman, D. Schlegel, and G. Skibinski, "System electrical parameters and their effects on bearing currents," *IEEE Transactions on Industry Applications*, vol. 33, pp. 577–584, Mar 1997.
- [65] A. Harnoy, *Bearing design in machinery: engineering tribology and lubrication*. CRC press, 2002.
- [66] A. Muetze and A. Binder, "Calculation of circulating bearing currents in machines of inverter-based drive systems," in *Conference Record of the 2004 IEEE Industry Applications Conference, 2004. 39th IAS Annual Meeting.*, vol. 2, pp. 720–726 vol.2, Oct 2004.
- [67] A. Muetze and A. Binder, "Experimental evaluation of mitigation techniques for bearing currents in inverter-supplied drive-systems - investigations on induction motors up to 500 kW," in *Electric Machines and Drives Conference, 2003. IEMDC'03. IEEE International*, vol. 3, pp. 1859–1865 vol.3, June 2003.
- [68] H. D. Gersem and A. Muetze, "Finite-element supported transmission-line models for calculating high-frequency effects in machine windings," *IEEE Transactions on Magnetics*, vol. 48, pp. 787–790, Feb 2012.
- [69] O. A. Mohammed, S. Ganu, N. Abed, S. Liu, and Z. Liu, "High frequency PM synchronous motor model determined by FE analysis," *IEEE Transactions on Magnetics*, vol. 42, pp. 1291–1294, April 2006.
- [70] O. A. Mohammed and S. Ganu, "FE-circuit coupled model of electric machines for simulation and evaluation of EMI issues in motor drives," *IEEE Transactions on Magnetics*, vol. 46, pp. 3389–3392, Aug 2010.
- [71] M. Wright, S. Yang, and K. McLeay, "General theory of fast-fronted interturn voltage distribution in electrical machine windings," in *IEE Proceedings B (Electric Power Applications)*, vol. 130, pp. 245–256, IET, 1983.

- [72] G. Suresh, H. A. Toliyat, D. A. Rendussara, and P. N. Enjeti, "Predicting the transient effects of PWM voltage waveform on the stator windings of random wound induction motors," in *Proceedings of APEC 97 - Applied Power Electronics Conference*, vol. 1, pp. 135–141 vol.1, Feb 1997.
- [73] H. V. Jorjks, E. Gjonaj, T. Weiland, and O. Magdun, "Three-dimensional simulations of an induction motor including eddy current effects in core laminations," *IET Science, Measurement Technology*, vol. 6, pp. 344–349, September 2012.
- [74] H. D. Gerssem, O. Henze, T. Weiland, and A. Binder, "Transmission-line modelling of wave propagation effects in machine windings," in *2008 13th International Power Electronics and Motion Control Conference*, pp. 2385–2392, Sept 2008.
- [75] D. Zhang, L. Kong, and X. Wen, "High frequency model of interior permanent magnet motor for EMI analysis," in *2014 IEEE Conference and Expo Transportation Electrification Asia-Pacific (ITEC Asia-Pacific)*, pp. 1–6, Aug 2014.
- [76] B. Mirafzal, G. Skibinski, R. Tallam, D. Schlegel, and R. Lukaszewski, "Universal induction motor model with low-to-high frequency response characteristics," in *Conference Record of the 2006 IEEE Industry Applications Conference Forty-First IAS Annual Meeting*, vol. 1, pp. 423–433, Oct 2006.
- [77] O. Magdun, S. Blatt, and A. Binder, "Calculation of stator winding parameters to predict the voltage distributions in inverter fed AC machines," in *2013 9th IEEE International Symposium on Diagnostics for Electric Machines, Power Electronics and Drives (SDEMPED)*, pp. 447–453, Aug 2013.
- [78] D. Meeker, "Continuum representation of wound coils via an equivalent foil approach," Available on 1-5-2015 at [Http://www.femm.info/examples/prox/notes.pdf](http://www.femm.info/examples/prox/notes.pdf), 2010.
- [79] O. Magdun and A. Binder, "An iron core impedance model for calculating high frequency common mode currents and shaft voltages in inverter-fed AC machines," in *International Symposium on Power Electronics Power Electronics, Electrical Drives, Automation and Motion*, pp. 135–140, June 2012.
- [80] P. Maeki-Ontto and J. Luomi, "Common mode flux calculation of AC machines," in *Proc. 15th Int. Conf. Electr. Mach. Drives (ICEM)*, 2002.
- [81] S. Duchesne, G. Parent, J. Moeneclay, and D. Roger, "Prediction of PDIV in motor coils using finite element method," in *2016 IEEE International Conference on Dielectrics (ICD)*, vol. 2, pp. 638–641, July 2016.

- [82] V. Mihaila, S. Duchesne, D. Roger, and P. Y. Liegeois, “Prediction of the turn-to-turn voltages in parallel connected wires configuration for motor coils fed by steep fronted pulses,” in *2011 Electrical Insulation Conference (EIC)*., pp. 407–412, June 2011.
- [83] V. Mihaila, S. Duchesne, and D. Roger, “A simulation method to predict the turn-to-turn voltage spikes in a PWM fed motor winding,” *IEEE Transactions on Dielectrics and Electrical Insulation*, vol. 18, pp. 1609–1615, October 2011.
- [84] A. T. Brahimi, A. Foggia, and G. Meunier, “End winding reactance computation using a 3D finite element program,” *IEEE Transactions on Magnetics*, vol. 29, pp. 1411–1414, Mar 1993.
- [85] M. Bortolozzi, A. Tessarolo, and C. Bruzzese, “Analytical computation of end-coil leakage inductance of round-rotor synchronous machines field winding,” *IEEE Transactions on Magnetics*, vol. 52, pp. 1–10, Feb 2016.
- [86] D. Ban, D. Zarko, and I. Mandic, “Turbogenerator end winding leakage inductance calculation using a 3-D analytical approach based on the solution of neumann integrals,” in *Electric Machines and Drives Conference, 2003. IEMDC’03. IEEE International*, vol. 3, pp. 1576–1582 vol.3, June 2003.
- [87] L. Middelstaedt, D. Richter, A. Lindemann, and A. Wintrich, “Influence of the configuration of the load cable on switching characteristics of IGBTs,” in *PCIM Europe 2016; International Exhibition and Conference for Power Electronics, Intelligent Motion, Renewable Energy and Energy Management*, pp. 1–8, May 2016.
- [88] D. Richter, *Detaillierte Untersuchung des Schaltverhaltens von Leistungshalbleitern bei langem Motorkabel*. Otto von Guericke Universitt Magdeburg, 2016.
- [89] A. Wintrich and R. Weiss, “Influence of capacitive cable load on switching losses,” Jan 2017.
- [90] A. Wintrich, “Verhaltensmodellierung von leistungshalbleitern für den rechnergestützten entwurf leistungselektronischer schaltungen,” *Power*, vol. 124, pp. 5–1, 1997.
- [91] N. Aoki, K. Satoh, and A. Nabae, “Damping circuit to suppress motor terminal overvoltage and ringing in PWM inverter-fed AC motor drive systems with long motor leads,” *IEEE Transactions on Industry Applications*, vol. 35, pp. 1014–1020, Sep 1999.
- [92] A. von Jouanne, D. Rendusara, P. Enjeti, and W. Gray, “Filtering techniques to minimize the effect of long motor leads on pwm inverter fed ac motor drive systems,” in *IAS ’95. Conference Record of the 1995 IEEE*

Industry Applications Conference Thirtieth IAS Annual Meeting, vol. 1, pp. 37–44 vol.1, Oct 1995.

- [93] A. von Jouanne and P. Enjeti, “Design considerations for an inverter output filter to mitigate the effects of long motor leads in ASD applications,” in *Applied Power Electronics Conference and Exposition, 1996. APEC '96. Conference Proceedings 1996., Eleventh Annual*, vol. 2, pp. 579–585 vol.2, Mar 1996.
- [94] Han-Jong Kim, Geun-Ho Lee, Cheol-Ho Jang, Jea-Pil Lee, and Jong-Ho Seo, “Cost-effective design of an inverter output reactor in asd applications,” in *IECON'99. Conference Proceedings. 25th Annual Conference of the IEEE Industrial Electronics Society (Cat. No.99CH37029)*, vol. 1, pp. 204–209 vol.1, Nov 1999.
- [95] A. F. Moreira, T. A. Lipo, G. Venkataramanan, and S. Bernet, “High frequency modeling for cable and induction motor overvoltage studies in long cable drives,” in *Conference Record of the 2001 IEEE Industry Applications Conference. 36th IAS Annual Meeting (Cat. No.01CH37248)*, vol. 3, pp. 1787–1794 vol.3, Sep. 2001.
- [96] J. He, G. Y. Sizov, P. Zhang, and N. A. O. Demerdash, “A review of mitigation methods for overvoltage in long-cable-fed PWM AC drives,” in *2011 IEEE Energy Conversion Congress and Exposition*, pp. 2160–2166, Sep. 2011.
- [97] F. Castelli-Dezza, M. M. Maglio, G. Marchegiani, D. F. Ortega, and D. Rosati, “Reduction of motor overvoltage fed by PWM AC drives using a universal model,” in *The XIX International Conference on Electrical Machines - ICEM 2010*, pp. 1–6, Sep. 2010.
- [98] Y. Jiang, W. Wu, Y. He, H. S. H. Chung, and F. Blaabjerg, “New passive filter design method for overvoltage suppression and bearing currents mitigation in a long cable based PWM inverter-fed motor drive system,” *IEEE Transactions on Power Electronics*, vol. 32, pp. 7882–7893, Oct 2017.
- [99] F. Alhuwaishel, A. Morsy, and P. Enjeti, “A new active output filter (AOF) for variable speed constant frequency (VSCF) power system in aerospace applications,” in *2015 IEEE Energy Conversion Congress and Exposition (ECCE)*, pp. 5439–5446, Sept 2015.
- [100] W. Dai, P. Enjeti, and D. Qiu, “Advanced active output filter for low acoustic noise adjustable speed drive (ASD) system,” in *2016 IEEE 8th International Power Electronics and Motion Control Conference (IPEMC-ECCE Asia)*, pp. 3646–3653, May 2016.
- [101] S. Lee and K. Nam, “An overvoltage suppression scheme for AC motor drives using a half dc-link voltage level at each PWM transition,” *IEEE Transactions on Industrial Electronics*, vol. 49, pp. 549–557, Jun 2002.

- [102] T. G. Habetler, R. Naik, and T. A. Nondahl, "Design and implementation of an inverter output LC filter used for dv/dt reduction," *IEEE Transactions on Power Electronics*, vol. 17, pp. 327–331, May 2002.
- [103] B. Anirudh Acharya and V. John, "Design of output dv/dt filter for motor drives," in *2010 5th International Conference on Industrial and Information Systems*, pp. 562–567, July 2010.